

Steady-state fretting response governed by periodic stress variations induced by oblique excitation

Shenghao Lu(卢晟昊), Huan Wang(王欢), and Shaoze Yan(阎绍泽)
Citation: Chin. Phys. B, 2026, 35 (**1**): 014601. DOI: 10.1088/1674-1056/ae181b
http://cpb.iphy.ac.cn; http://iopscience.iop.org/cpb

What follows is a list of articles you may be interested in

Micro sliding friction model considering periodic variation stress distribution of contact surface and experimental verification

Sheng-Hao Lu(卢晟昊), Jing-Yu Han(韩靖宇), and Shao-Ze Yan(阎绍泽)
Chin. Phys. B, 2023, 32 (**4**): 044602. DOI: 10.1088/1674-1056/ac9043

Mechanism analysis and improved model for stick-slip friction behavior considering stress distribution variation of interface

Jingyu Han(韩靖宇), Jiahao Ding(丁甲豪), Hongyu Wu(吴宏宇), and Shaoze Yan(阎绍泽)
Chin. Phys. B, 2022, 31 (**3**): 034601. DOI: 10.1088/1674-1056/ac1931

Experimental analysis of interface contact behavior using a novel image processing method

Jingyu Han(韩靖宇), Zhijun Luo(罗治军), Yuling Zhang(张玉玲), and Shaoze Yan(阎绍泽)
Chin. Phys. B, 2021, 30 (**5**): 054601. DOI: 10.1088/1674-1056/abd696

Evolution of real contact area during stick-slip movement observed by total reflection method

Zhijun Luo(罗治军), Baojiang Song(宋保江), Jingyu Han(韩靖宇), Shaoze Yan(阎绍泽)
Chin. Phys. B, 2019, 28 (**10**): 104601. DOI: 10.1088/1674-1056/ab3f1f

Relationship between the real contact area and contact force in pre-sliding regime

Baojiang Song(宋保江), Shaoze Yan(阎绍泽)
Chin. Phys. B, 2017, 26 (**7**): 074601. DOI: 10.1088/1674-1056/26/7/074601

Steady-state fretting response governed by periodic stress variations induced by oblique excitation

Shenghao Lu(卢晟昊)[1], Huan Wang(王欢)[2], and Shaoze Yan(阎绍泽)[1,†]

[1] *State Key Laboratory of Tribology, Department of Mechanical Engineering, Tinghua University, Beijing* 100084, *China*
[2] *School of Engineering and Technology, China University of Geosciences (Beijing), Beijing* 100083, *China*

(Received 20 August 2025; revised manuscript received 30 September 2025; accepted manuscript online 28 October 2025)

This study investigates the mechanisms of friction-induced vibration under periodic variations in stress distribution using an improved fretting friction model. A fretting friction test system integrated with a total reflection method was developed to analyze interfacial contact behavior under dynamic loading conditions. An improved fretting friction model was established, incorporating three critical nonlinear parameters: the hysteretic friction coefficient, tangential stiffness fluctuations, and stress distribution. Through systematic validation, the model demonstrates high-fidelity replication of experimental steady-state amplitude–frequency responses. Key findings reveal that non-uniform stress distribution governs irregularities in the vibration response, and increased uniformity intensifies stick–slip instabilities. Near the stick–slip transition threshold, distinct vibration anomalies emerge due to the coupled effects of stress heterogeneity, friction hysteresis, and stiffness variations during state transitions. Furthermore, the magnitude of the normal contact force systematically alters the dominant interfacial contact mechanism. The different interfacial contact states at various frequencies lead to distinct steady-state responses. This shift elevates resonance frequencies and amplifies higher-order resonant peaks. The fretting friction model provides a predictive framework for vibration control under dynamic interfacial loading.

Keywords: total reflection method, stress distribution, the fretting friction model, normal force, stick–slip

PACS: 46.55.+d, 42.30.Va, 43.40.Ga

DOI: 10.1088/1674-1056/ae181b **CSTR:** 32038.14.CPB.ae181b

1. Introduction

Fretting is a frictional contact phenomenon that leads to damage at the contact region between two nominally clamped surfaces subjected to oscillatory motion of small amplitudes. The region of contact between the blade and the disk at the dovetail joint is one of the critical locations for fretting damage.[1]

High-cycle fatigue failure in aero-engine turbine blades is frequently caused by blade resonance. Mitigating this risk requires analyzing the blade vibration response. Blade dampers suppress vibration by dissipating energy through dry friction at the blade root–damper interface. However, the contact friction force models currently employed in vibration response analysis often insufficiently account for the nonlinear effects of the interface parameters.[2]

In analyzing the vibration response of mechanical structures with contact interfaces, numerous experimental and theoretical studies have been conducted. Pesaresi *et al.*[3,4] developed a nonlinear dynamic modeling approach for blade–damper systems and designed a dedicated test bench to evaluate damper performance. Menq *et al.*[5] formulated nonlinear functions relating elliptical motion to nonlinear spring resistance and friction damping, employing a single-term harmonic balance method to compute the resonance response of a frictionally constrained two-degree-of-freedom oscillator. Joannin *et al.*[6] performed nonlinear modal analysis on a simplified blade–disk model with dry friction, revealing that structural mistuning affects nonlinear modal characteristics and demonstrating an optimal mistuning amplitude for vibration attenuation under specific mistuning patterns. She *et al.*[7] established a continuum model using specialized modal functions to simulate rotating beams with loose dovetail joints, identifying softening nonlinearity in the amplitude–frequency curves at low rotational speeds and noting significant damping effects arising from higher excitation levels and friction coefficients.

Zhao *et al.*[8] analyzed mistuning effects by varying tangential interface stiffness, initial shroud clearance (governing normal preload), and blade structural stiffness. This work revealed complex nonlinear vibrations in frictionally coupled blade–disk systems, showing that smaller normal preloads combined with larger force variations can substantially reduce the response amplitudes of mistuned blades. Asai *et al.*[2,9] designed a two-dimensional friction test system and experimentally demonstrated that periodically varying normal forces dissipate more energy than constant normal forces when the tangential force coefficient is below the sliding friction coefficient. Studies have shown that the complex mechanical behavior between interfaces leads to nonlinear phenomena in energy dissipation and stiffness, thereby affecting the dynamic

†Corresponding author. E-mail: yansz@mail.tsinghua.edu.cn

© 2026 Chinese Physical Society and IOP Publishing Ltd. All rights, including for text and data mining, AI training, and similar technologies, are reserved.

characteristics of the entire mechanical structure. This phenomenon is related to non-uniform stress distributions induced by normal force fluctuations.[10]

Vingsbo and Soderberg[11] proposed a three-stage theory of fretting wear, identifying contact stress concentration as the primary cause of crack initiation and establishing a quantitative relationship between wear rate and slip amplitude, laying the foundation for subsequent studies. Researchers have found a power-law relationship between energy dissipation and the amplitude of tangential fluctuations. Goodman[12] investigated analytical solutions to elastic frictional contact under oscillating shear loads and found that the power-law exponent between energy dissipation and the amplitude of tangential fluctuations is approximately 3.0. Usta *et al.*[13] examined the relationship between frictional energy dissipation and normal and tangential load parameters in spherical contacts, discovering that the power-law exponent is 2.49 under constant normal loads and varies under different normal load fluctuations, approaching 2 under no-load conditions. These results indicate that the power-law exponent between energy dissipation and the amplitude of tangential fluctuations is not constant. Xiao *et al.*[14] adopted a one-dimensional micro-slip friction model incorporating interfacial tangential stiffness and derived load–force–displacement curves under varying pressure distribution patterns and interfacial tangential stiffness values. Their analysis revealed that the power-law exponent linking energy dissipation to the amplitude of tangential fluctuations depends on both the interfacial tangential stiffness and the pressure distribution pattern.

Currently, the main micro-slip friction models include the Valanis model,[15] the Bouc–Wen model,[16] and the Iwan model,[17] among others. The Iwan model consists of a series of Jenkins elements connected in parallel or series, allowing consideration of more nonlinear contact parameters. The model can be refined by modifying the characteristics and number of Jenkins elements, enabling a more precise description of contact behavior. Consequently, the Iwan model is widely used in the dynamic analysis of contact interfaces.[18,19]

Interface contact visualization techniques mainly include ultrasonic, pressure-film, and optical methods, among which the optical method is the longest established and most widely used.[20,21] Due to the difference in refractive indices between air and the contacting bodies, bright and dark regions appear within the contact area at suitable observation angles, reflecting the distribution and evolution of the real contact area. Maegawa *et al.*[22–25] considered factors such as contact angle and specimen dimensions to examine changes in precursor wavelength during the pre-slip phase of viscous sliding friction.

Song *et al.*[26,27] proposed an experimental method based on optical total reflection to measure the true contact area of transparent contact blocks. Images projected onto a screen were captured using a digital single-lens reflex (DSLR) camera, and an improved Otsu algorithm was introduced to process the images. Luo *et al.*[28,29] developed an experimental system based on the optical total reflection method, observed changes in the real contact area of polymethyl methacrylate (PMMA) during viscous sliding, and found that the real contact area increases with tangential force. This setup can also be used to validate contact models. Han *et al.*[30,31] proposed a visualization technique for analyzing interfacial contact behavior using optical total reflection. Lu *et al.*[32] constructed a two-dimensional vibration test bench based on Asai's experimental device and the total reflection method. Feng *et al.*[33] presented a comprehensive analysis of fretting wear under wind-induced vibration, providing a reference for mechanical equipment design and protection.

To prevent fretting wear at contact interfaces, guide the design of advanced mechanical equipment, and extend service life, this paper conducts the following work. Fretting friction experiments were carried out using the optical total reflection method, where grayscale images of the contact area characterized variations in interfacial stress distribution. Based on these observations, an improved fretting friction model is proposed. This model investigates the influence of nonlinear contact parameters on amplitude–frequency curves. These curves are subsequently employed to analyze variations in interfacial contact states under different normal loads and to examine the mechanisms governing stick–slip transitions.

2. Experimental methodology and analysis

In practical engineering, contact interfaces are frequently subjected to inclined excitation. To simulate this scenario, a harmonic excitation force F_α is applied to specimen 1 at an angle α relative to the x-direction of the contact interface, while specimen 2 is rigidly constrained, as shown in Fig. 1(a). F_α can be decomposed into the normal force F_n and the tangential force F_t. The relative displacement of specimen 1 along the x-direction with respect to specimen 2 is δ.

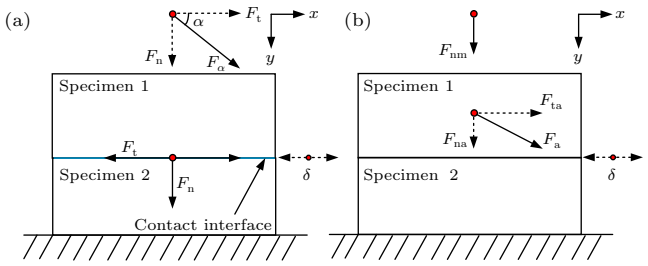


Fig. 1. Schematic diagram of tilting vibration at an angle α between the excitation and the contact interface.

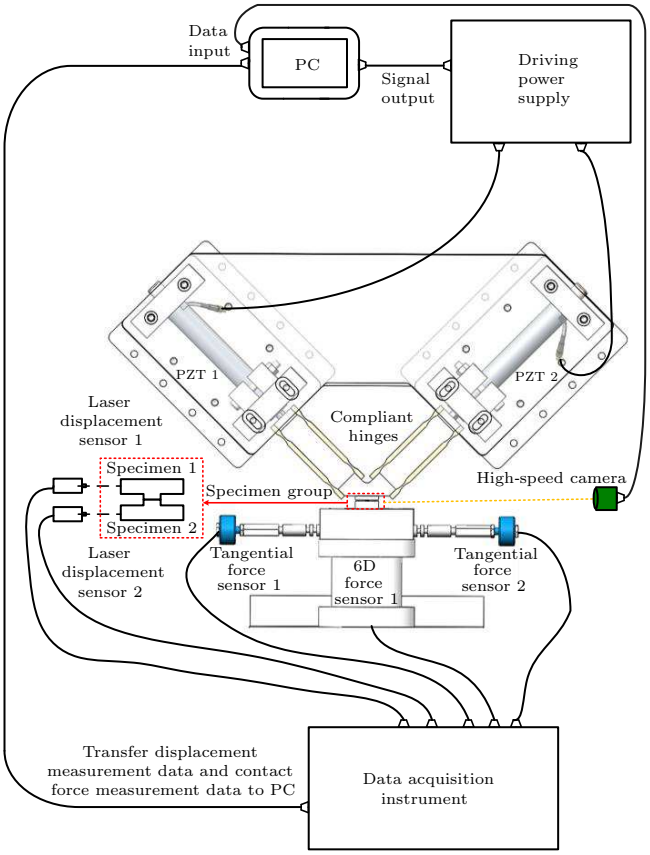


Fig. 2. Schematic wiring diagram of the fretting friction test system.

When there is an angle between the excitation and the interface, the loading can be represented as a two-dimensional coupled excitation, in which both the normal force and the tangential force applied to the contact interface fluctuate dynamically over time. The mean value of the tangential force F_t is $F_{tm} = 0$ N, with an amplitude of F_{ta}, while the mean value of the normal force F_n is F_{nm}, with an amplitude of F_{na}. These fluctuating forces together create a complex contact condition that closely simulates real-world fretting scenarios.

Drawing on Asai's experimental protocol[2,9] and the total reflection method,[34] a fretting friction test system was established, as shown in Fig. 2.

This system comprises three main components: the control module, the actuator unit, and the signal acquisition module. The specific parameters of the key equipment are listed in Table 1. The driving power supply, controlled by a PC, outputs two signals whose amplitude, frequency, and phase can be adjusted independently to accurately replicate coupled excitations. The actuator unit includes two piezoelectric stack actuators (PZTs) and four compliant hinges. Each PZT generates fluctuating normal and tangential forces on the contact specimen through its associated compliant hinge. Because piezoelectric stacks cannot withstand tensile loads, each actuator is internally preloaded with a spring plate within its metal housing. This preload force is set to 10% (470 N) of the maximum compressive force the actuator can provide. The signal acquisition module includes two laser displacement sensors, a six-dimensional (6D) force sensor, two tangential force sensors, a high-speed camera, and a laser device, enabling precise monitoring of the fretting process.

The fretting friction test bench is shown in Fig. 3(a). The specimen assembly consists of specimen 1 and specimen 2. The specimen materials are PMMA and stainless steel (SUS304). Both specimen 1 and specimen 2 are designed with double-boss structures, as shown in Fig. 3(b), ensuring stable contact and uniform load distribution during testing.

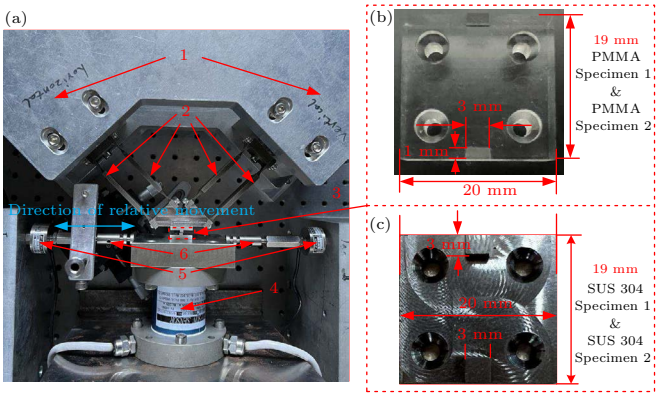


Fig. 3. Fretting friction test bench. (a) Components of the test bench: 1-piezoelectric actuators 1 and 2, 2-compliant hinges, 3-specimen group, 4-6D force sensor, 5-tangential force sensors 1 and 2, 6-rod and shaft. (b) Dimensions of PMMA specimens 1 and 2. (c) Dimensions of SUS304 specimens 1 and 2.

Table 1. Parameters of the main equipment.

Name of the equipment	Equipment model	Specific parameter
Tangential force sensor	BUFSON BSLM-3	accuracy/range: 0.5 N/500 N
6D force sensor	BUFSON BSFY-3	accuracy: 0.1% range
		$F_x = F_y = 600$ N
		range: $F_z = 1000$ N
		$M_x = M_y = 10$ N·m
Laser displacement sensor	KEYNCE LK-H020	accuracy/range: 0.1 μm/5 mm
Data acquisition device	ECON MI-7016	number of channels: 16
		maximum sampling frequency: 100 kHz
Piezoelectric actuator	PST150/14/120VS20	stroke 125.616 μm, stiffness 35 N/μm, capacitance 47 μF
Driving power supply	E00.C2	frequency range: 2 Hz to 110 Hz
High-speed camera	M110-12G	maximum frames per second: 6000

Contact area imaging is performed using the total reflection method,[34] as shown in Fig. 4(a). When a laser beam propagates from a higher-refractive-index medium (PMMA in this experiment) to a lower-refractive-index medium (air), total internal reflection occurs if the incidence angle exceeds the critical angle. In fretting friction experiments, when two transparent PMMA specimens come into contact, incident light from the source reaches the interface. At asperity contact zones, the laser light transmits through the interface, whereas in non-contact regions containing air-filled cavities, total reflection occurs. The transmitted light intensity is proportional to the true asperity contact area. The size and morphology of the contact spots evolve in real time, synchronizing with dynamic variations in the interfacial stress distribution.

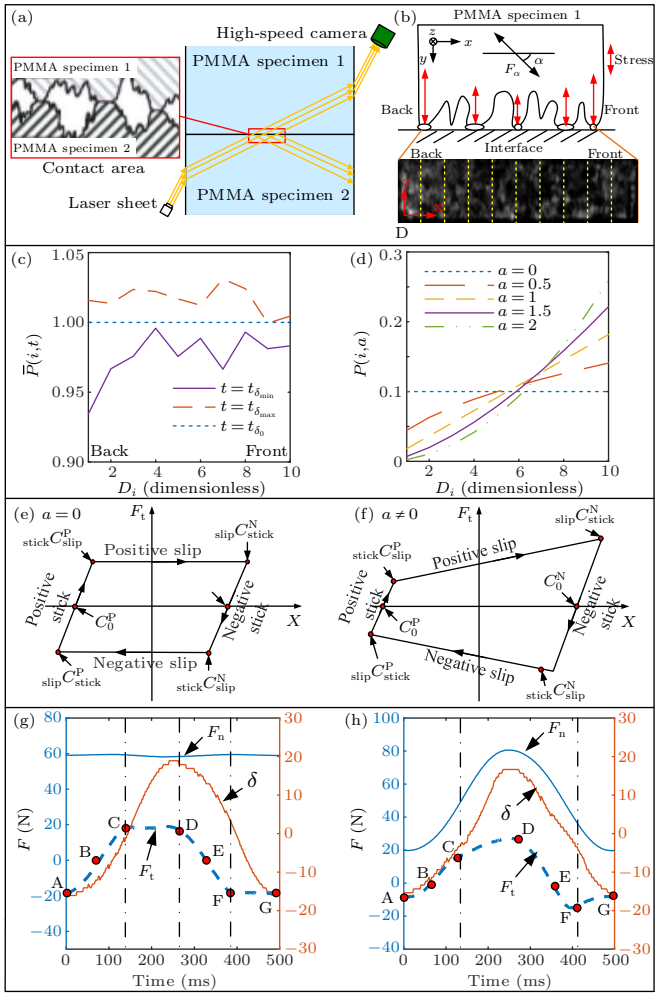


Fig. 4. Observation of contact interface stress distribution via total internal reflection and its effect on hysteresis loop characteristics. (a) Schematic of the total reflection method. (b) Original grayscale image of the contact interface at excitation angle α. (c) Experimentally measured stress distributions at varying relative displacements. (d) Equivalent stress distribution based on the power function. (e) Hysteresis loop under uniform normal stress distribution. (f) Hysteresis loop under heterogeneous normal stress distribution. (g) Time-domain motion plots under uniform normal stress distribution. (h) Time-domain motion plots under heterogeneous normal stress distribution.

During real contact area observation, specimen 1 undergoes reciprocating lateral displacement relative to fixed specimen 2. The high-speed camera remains stationary relative to specimen 2. Laser light emitted from the source undergoes both transmission and total reflection at the contact interface. The high-speed camera, operating at a 1000 fps acquisition frequency, records these interfacial contact images. Due to the camera's 64° observation angle, dimensional compression by a factor of 3.5 occurs along the z-axis. The original grayscale image is obtained by stretching the z-axis of the grayscale data by a factor of 3.5, as shown in Fig. 4(b). For each video frame, the grayscale image intensity matrix $I(x,z,t)$ is extracted, where pixel coordinates are denoted by x and z. The contact image intensity $I(x,z,t)$ at time t is expressed by Eq. (1),[32] where m and n are the row and column sizes of the image intensity matrix. The primary change in contact area occurs along the x-direction. The intensity distribution $I(x,t)$ in the x-direction is obtained by summing the image intensity along the z-direction, as shown in Eq. (2).[32]

$$I_{\text{sum}}(t) = \sum_{x=1}^{n}\sum_{z=1}^{m} I(x,z,t), \tag{1}$$

$$I(x,t) = \sum_{z=1}^{m} I(x,z,t). \tag{2}$$

The equivalent stress distribution $\bar{P}(x,t)$ along the x-direction of the interface is expressed by Eq. (3).[32] The contact zone is equally partitioned into ten segments along the x-direction, designated D_1 to D_{10}. The measured light intensity within each segment D_i is proportional to the local normal stress, as shown in Fig. 4(b)

$$\bar{P}(x,t) = \frac{\sum_{z=1}^{m} I(x,z,t)}{\sum_{z=1}^{m} I(x,z,0)}. \tag{3}$$

Distinct equivalent stress distributions $\bar{P}(x,t)$ correspond to different relative displacements δ, where t_{δ_0} denotes the instant of zero relative displacement, $t_{\delta_{\max}}$ the instant of maximum displacement, and $t_{\delta_{\min}}$ the instant of minimum displacement, as shown in Fig. 4(c). $\bar{P}(x,t)$ is discretized and normalized to obtain $P(i,a)$, as defined in Eq. (4), where a represents the stress distribution coefficient characterizing interfacial stress heterogeneity. This coefficient governs the spatial evolution of stress: uniform normal stress distribution occurs at $a = 0$, linear stress increase from one end of the interface to the other occurs at $a = 1$, sublinear growth appears at $a = 0.5$, superlinear growth appears at $a = 1.5$, and quadratic growth appears at $a = 2$. The distributions $P(i,a)$ for different a values are compared in Fig. 4(d)

$$P(i,a) = i^a \left(\sum_{i=1}^{N} i^a\right)^{-1}, \quad (i = 1,2,\ldots,N). \tag{4}$$

Based on the characteristics of the hysteresis curve,[32] it is categorized into positive and negative segments, where

the sign corresponds to the direction of relative displacement. The positive segment contains positive stick and positive slip, while the negative segment contains negative stick and negative slip. At $a = 0$, the hysteresis loop exhibits an approximately parallelogram-like shape, as shown in Fig. 4(e). Stage-specific state transition points are denoted by ${}_{\text{sub}_\text{l}}C^{\text{sup}}_{\text{sub}_\text{r}}$: the superscript (sup) indicates the current displacement direction, the right subscript (sub_r) denotes the subsequent state, and the left subscript (sub_l) denotes the preceding state. The four critical transition points are labeled ${}_{\text{slip}}C^{\text{P}}_{\text{stick}}$, ${}_{\text{stick}}C^{\text{P}}_{\text{slip}}$, ${}_{\text{slip}}C^{\text{N}}_{\text{stick}}$, and ${}_{\text{stick}}C^{\text{N}}_{\text{slip}}$. Points with zero friction, referred to as friction zeros, are labeled C_0^{P} and C_0^{N} based on the direction of motion. When $a \neq 0$, asymmetric friction coefficients arise between positive and negative sliding phases due to stress heterogeneity,[32] causing the hysteresis loop to deviate from a parallelogram-like morphology. As a result, the transition points no longer coincide with characteristic quadrilateral vertices, as illustrated in Fig. 4(f). Time-domain plots of motion under uniform normal stress distribution are shown in Fig. 4(g), and those under heterogeneous normal stress distribution are shown in Fig. 4(h).

3. Improved fretting friction model

Building on Sanliturk's vibration analysis method,[35] a fretting friction model was developed to describe the nonlinear evolution of contact parameters arising from stress distribution fluctuations. The model incorporates periodically varying stress distributions under broadband frequency excitation, as validated in Fig. 5.

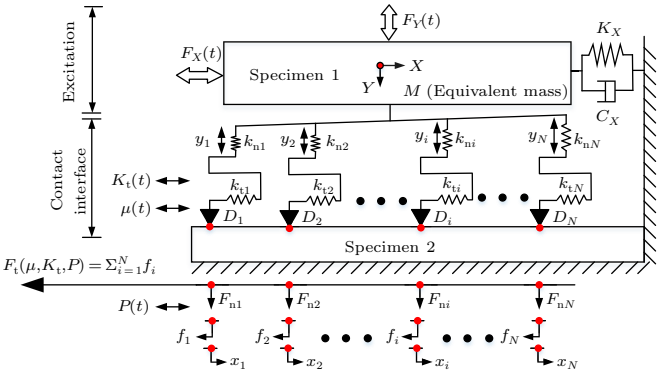


Fig. 5. Fretting friction model accounting for contact parameter fluctuations caused by stress variations.

The stress distribution is simulated by N Jenkins spring–slider elements in parallel. F_{n_i} denotes the normal force acting on the i-th Jenkins element, and y_i represents the compression of the normal spring under the influence of F_{n_i}. Each element consists of a normal spring (stiffness $k_{\text{n}i}$), a tangential spring (stiffness $k_{\text{t}i}$), and a damping slider D_i with friction force f_i; x_i corresponds to the displacement of D_i. Notably, the normal and tangential stiffnesses exhibit no coupling effects. Specimen 2 remains rigidly constrained, while specimen 1 is kinematically coupled to a fixed boundary through a parallel spring–damper system with linear stiffness K_X and viscous damping coefficient C_X. The equivalent mass of specimen 1 is represented by M.

Specimen 1 undergoes normal-direction sinusoidal excitation F_Y and tangential-direction sinusoidal excitation F_X, governed by Eqs. (5) and (6), respectively.

$$F_Y = F_{Y\text{m}}\left(1 + R_{F_Y}\sin(2\pi\omega t + \phi_{F_Y})\right), \tag{5}$$

$$F_X = F_{X\text{a}}\sin(2\pi\omega t + \phi_{F_X}), \tag{6}$$

where $F_{Y\text{m}}$ is the mean value of F_Y, and $F_{X\text{a}}$ is the amplitude of F_X. R_{F_Y} denotes the normal force fluctuation coefficient, and ϕ_{F_Y} and ϕ_{F_X} represent the initial phases. The mean value of the normal contact force F_{nm} equals the mean value of the normal excitation $F_{Y\text{m}}$, as shown in Eq. (7).

$$F_{\text{nm}} = F_{Y\text{m}}. \tag{7}$$

The no-load tangential displacement of specimen 1 is defined as X_0, and the no-load normal displacement as Y_0, expressed by Eqs. (8) and (9), respectively.

$$X_0 = X_{\text{m}} + X_{\text{a}}\sin(2\pi\omega t), \tag{8}$$

$$Y_0 = Y_{\text{m}} + Y_{\text{a}}\sin(2\pi\omega t), \tag{9}$$

where X_{m} and X_{a} are the mean value and amplitude of the tangential displacement, and Y_{m} and Y_{a} represent the mean value and amplitude of the normal displacement.

The interfacial friction force F_{t} is the aggregate of the friction forces f_i from all D_i, as formulated in Eq. (10). Similarly, the critical friction F_{c} corresponds to the sum of the critical friction forces $f_{\text{c}i}$ across all D_i, as given in Eq. (11).

$$F_{\text{t}} = \sum_{i=1}^{N} f_i, \tag{10}$$

$$F_{\text{c}} = \sum_{i=1}^{N} f_{\text{c}i}. \tag{11}$$

Considering the hysteresis of friction when $a \neq 0$, the direction of the frictional force f_i at point D_i is determined by the direction of acceleration. The transition criteria for the four states are presented in Eq. (12) and further elaborated in Eq. (13), where $x_{i,\text{rev}}$ and $f_{i,\text{rev}}$ denote the displacement and friction force at point D_i when the state velocity becomes zero.

$$\begin{aligned}
&{}_{\text{stick}}C^{\text{P}}_{\text{slip}}:\ f_{\text{t}i}(t) \geq f_{\text{c}i}(t) \text{ and } k_{\text{t}i}(t)\dot{X}(t) - \dot{f}_{\text{c}i}(t) > 0,\\
&{}_{\text{stick}}C^{\text{N}}_{\text{slip}}:\ f_{\text{t}i}(t) \leq -f_{\text{c}i}(t) \text{ and } k_{\text{t}i}(t)\dot{X}(t) + \dot{f}_{\text{c}i}(t) < 0,\\
&{}_{\text{slip}}C^{\text{P}}_{\text{stick}}:\ \dot{X}(t) + \dot{f}_{\text{c}i}(t)/k_{\text{t}i}(t) \geq 0 \text{ and } \ddot{X}(t) + \ddot{f}_{\text{c}i}(t)/k_{\text{t}i}(t) > 0,\\
&{}_{\text{slip}}C^{\text{N}}_{\text{stick}}:\ \dot{X}(t) - \dot{f}_{\text{c}i}(t)/k_{\text{t}i}(t) \leq 0 \text{ and } \ddot{X}(t) - \ddot{f}_{\text{c}i}(t)/k_{\text{t}i}(t) < 0,
\end{aligned} \tag{12}$$

$$f_i = \begin{cases} f_{ci} & {}_{\text{stick}}C^{\text{P}}_{\text{slip}} \to {}_{\text{slip}}C^{\text{N}}_{\text{stick}}, \\ -f_{ci} & {}_{\text{stick}}C^{\text{N}}_{\text{slip}} \to {}_{\text{slip}}C^{\text{P}}_{\text{stick}}, \\ k_{ti}(X(t)-x_{i,\text{rev}})+f_{i,\text{rev}} & {}_{\text{slip}}C^{\text{P}}_{\text{stick}} \to {}_{\text{stick}}C^{\text{P}}_{\text{slip}}, \\ k_{ti}(X(t)-x_{i,\text{rev}})+f_{i,\text{rev}} & {}_{\text{slip}}C^{\text{N}}_{\text{stick}} \to {}_{\text{stick}}C^{\text{N}}_{\text{slip}}, \end{cases} \tag{13}$$

where $f_{ti}(t)$ is the tangential force of D_i, $f_{ci}(t)$ is the critical frictional force of D_i, and $k_{ti}(t)$ is the tangential stiffness of D_i.

When $\phi_{F_Y} = 0^\circ$ and $\phi_{F_X} = 0^\circ$, Eqs. (4) and (14) govern the non-uniform equivalent stress fluctuations induced by normal force variations. The stress distribution coefficient a is jointly determined by the mean coefficient a_{m} and the amplitude coefficient a_{a}. Utilizing Eqs. (4) and (14), the equivalent load F_{n_i} at point D_i can be derived, as given in Eq. (16).

$$a = a_{\text{m}} + a_{\text{a}}\sin(2\pi\omega t), \tag{14}$$

$$F_{\text{n}} = F_{\text{nm}}\left(1 + R_{\text{na}}\sin(2\pi\omega t)\right), \tag{15}$$

$$F_{\text{n}_i} = F_{\text{n}} \times P(i,a) = F_{\text{nm}}P(i,a)\left(1 + R_{\text{na}}\sin(2\pi\omega t)\right), \tag{16}$$

where R_{na} represents the normal force fluctuation coefficient.

The friction coefficient $\mu(t)$ incorporates hysteresis effects, with μ_{p} denoting its value in the positive sliding regime and μ_{n} in the negative sliding regime. The friction force f_{ci} is governed by the normal force $F_{\text{n}i}$ on D_i and the regime-specific friction coefficient, as defined in Eq. (17) for the positive sliding regime and Eq. (18) for the negative sliding regime. The ratio of negative to positive friction coefficient is R_μ, given by Eq. (19).

$$f^{\text{P}}_{ci} = F_{\text{n}i}\mu_{\text{P}}, \tag{17}$$

$$f^{\text{N}}_{ci} = -F_{\text{n}i}\mu_{\text{N}}, \tag{18}$$

$$\mu_{\text{N}} = R_\mu\mu_{\text{P}}. \tag{19}$$

$K_{\text{t}}(t)$ denotes the interfacial tangential stiffness that incorporates the effect of fluctuating normal loads. Experimental analysis provides the value of K_{t} under different orientation angles α, as shown in Eq. (20). When the resultant interfacial contact force acts at an angle α_0 to the interface, the tangential stiffness is identical in both sliding regimes and can be experimentally determined. R_{K} is the stiffness fluctuation coefficient. The interfacial tangential stiffness K_{t} increases with normal force but does not exceed the structural tangential stiffness K_X. When $K_{\text{t}} \geq K_X$, the displacement at the contact interface equals that of specimen 1, and K_{t} consequently takes the value of K_X. The mean tangential stiffness K_{tm} is linearly dependent on the mean normal force F_{nm}, as given in Eq. (21). The friction-coefficient behavior is analogous and is formulated in Eq. (22).

$$K_{\text{t}} = \begin{cases} K_{\text{tm}}\left(1 + R_{\text{K}}R_{\text{na}}\sin(2\pi wt)\right), & R_{\text{na}} \geq \mu\tan\alpha_0 \text{ and } K_{\text{t}} < K_X, \\ K_{\text{tm}}(1 - R_{\text{K}}R_{\text{na}}), & R_{\text{na}} < \mu\tan\alpha_0 \text{ and } K_{\text{t}} < K_X, \\ K_X, & K_{\text{t}} \geq K_X, \end{cases} \tag{20}$$

$$K_{\text{tm}} = p_1F_{\text{nm}} + p_2, \tag{21}$$

$$R_\mu = \begin{cases} p_3R_{\text{na}} + p_4, & R_{\text{na}} \geq \mu\tan\alpha_0, \\ 1, & R_{\text{na}} < \mu\tan\alpha_0, \end{cases} \tag{22}$$

where p_1, p_2, p_3, p_4, and R_{K} are determined from experimental parameter identification.

Based on the above analysis, the equation of motion for the fretting friction model is established, as shown in Eq. (23). $X(t)$ is the relative interfacial displacement

$$M\ddot{X} + C_X\dot{X} + K_XX(t) = F_X(t) - F_{\text{t}}(\mu(t), K_{\text{t}}(t), P(t)). \tag{23}$$

The tangential force F_{t} at the contact interface is calculated using Eq. (10). The friction force F_{t} incorporates the influence of three nonlinear parameters: the friction coefficient $\mu(t)$, the tangential stiffness $K_{\text{t}}(t)$, and the stress distribution $P(t)$. The friction coefficient $\mu(t)$ incorporates hysteresis effects, as defined in Eqs. (17)–(19). The interfacial tangential stiffness $K_{\text{t}}(t)$ accounts for stress-distribution fluctuations, governed by Eqs. (20)–(22). $P(t)$ represents the stress distribution induced by fluctuating normal force, as defined by Eqs. (4) and (14).

Table 2. Input parameters for the fretting friction model.

Parameter	Symbol	Parameter	Symbol
Normal force mean value	F_{nm}	Tangential stiffness mean value	K_{tm}
Normal force fluctuation coefficient	R_{F_Y}	Tangential stiffness fluctuation coefficient	R_{K}
Positive friction coefficien	μ_{P}	Stress distribution mean value coefficient	a_{m}
Negative friction coefficient	μ_{N}	Stress distribution amplitude coefficient	a_{a}
Displacement fluctuation amplitude	X_{a}	Excitation frequency	ω

Figure 6 schematizes the computational algorithm for the fretting friction model. Experimentally identified parameters serve as inputs, as shown in Table 2.

The output parameter is the steady-state response $\delta_{\text{SS}}(\omega)$, where the subscript SS denotes steady state. The relationship between $\delta_{\text{SS}}(\omega)$ and the relative interfacial displacement $X(t,\omega)$ is given by Eq. (24). Typically, $\delta_{\text{SS}}(\omega)$ corresponds to the amplitude of $X(t,\omega)$ extracted at the 100th-cycle time instant

$$\delta_{\text{SS}}(\omega) = \lim_{t\to\infty}\sup\left|X(t,\omega)\right|. \tag{24}$$

The steady-state response δ_{SS} varies with the excitation frequency ω. The curve plotting δ_{SS} against ω — with ω as the abscissa and δ_{SS} as the ordinate — is termed the

amplitude–frequency characteristic curve of the steady-state displacement response. This amplitude–frequency curve enables evaluation of interfacial stress distribution effects on system vibration characteristics, supports resonance risk assessment, and facilitates dynamic design optimization.

The solution sequence comprises: (i) stick–slip state determination, (ii) sliding-direction identification when applicable, (iii) Jenkins-element friction-force computation, (iv) assembly of the resultant interfacial friction force, (v) acceleration solution via the equations of motion, (vi) time-domain numerical integration to obtain velocity and interfacial displacement, and (vii) quantification of the steady-state fretting response by the interfacial displacement amplitude.

4. Fretting friction simulation analysis

4.1. Experimental identification of input parameters

In Section 2, experiments using the total reflection method were conducted with PMMA specimens to determine stress-distribution patterns at the contact interface. Given the widespread application of stainless steel in mechanical interfaces, SUS304 was adopted for parameter identification in this experimental phase. The resulting parameters for the fretting friction model were subsequently used in the simulation analyses.

The input parameters for the fretting friction model in Fig. 6 require experimental identification. External excitation frequencies applied by the PZT were set to 2 Hz, 10 Hz, 20 Hz, 30 Hz, 40 Hz, 50 Hz, 60 Hz, 70 Hz, 80 Hz, 90 Hz, 100 Hz, 110 Hz, and 120 Hz. Physical quantities, including normal contact force, tangential contact force, and relative displacement, were measured using the test bench in Fig. 2. These measurements were substituted into the equations in Fig. 6 for inverse analysis, yielding the contact parameters: $\alpha = 45°$, $M = 9.988$ kg, $K_X = 1.013 \times 10^7$ N/m, $C_X = 202.236$ N·s/m, $K_{\mathrm{tm}} = 3.006 \times 10^6$ N/m, $\mu_{\mathrm{P}} = 0.36$, $\mu_{\mathrm{N}} = 0.42$, $X_{\mathrm{a}} = 2.842 \times 10^{-5}$ m, $R_{F_Y} = 0.49$, $R_{\mathrm{K}} = 0.13$, $\phi_{F_Y} = 0°$, $\phi_{F_X} = 0°$, $p_1 = 3.41 \times 10^4$, $p_2 = 3.88 \times 10^5$, $p_3 = 0.38$, and $p_4 = 1.09$. M represents the equivalent mass accounting for system constraints (e.g., compliant hinges).

Using these parameters with an excitation frequency of 2 Hz and normal force of 50 N, the micro-slip frictional vibration model calculated the system's dissipated energy E_{D} for Jenkins-element counts $N = 1$, 4, 7, 10, 20, 50, and 100. Results are shown in Fig. 7(a), with relative errors in Fig. 7(b). Higher N values require more computational resources. At $N = 10$, the relative error remains below 2.3%, satisfying accuracy requirements; therefore, $N = 10$ was adopted for subsequent simulations.

With experimentally identified parameters, we set $N = 10$, $a_{\mathrm{m}} = 0.5$, and $a_{\mathrm{a}} = 0.5$. Normal forces of 50 N, 100 N, 200 N, and 500 N were input into the fretting friction model program. Computational results are presented in Fig. 8(a). Using the test system in Fig. 2, maximum displacements were measured at excitation frequencies of 2 Hz, 6 Hz, 12 Hz, 24 Hz, 36 Hz, 48 Hz, 60 Hz, 72 Hz, 84 Hz, 96 Hz, 108 Hz, and 120 Hz, with results in Fig. 8(b). Lines in Fig. 8(b) denote simulation data from Fig. 8(a).

At $a_{\mathrm{m}} = 0.5$ and $a_{\mathrm{a}} = 0.5$, the coefficient of determination R^2 reaches 0.961 for normal forces of 50 N, 100 N, 200 N, and 500 N, demonstrating excellent agreement between simulation and experimental data and validating the model's capability to replicate observations.

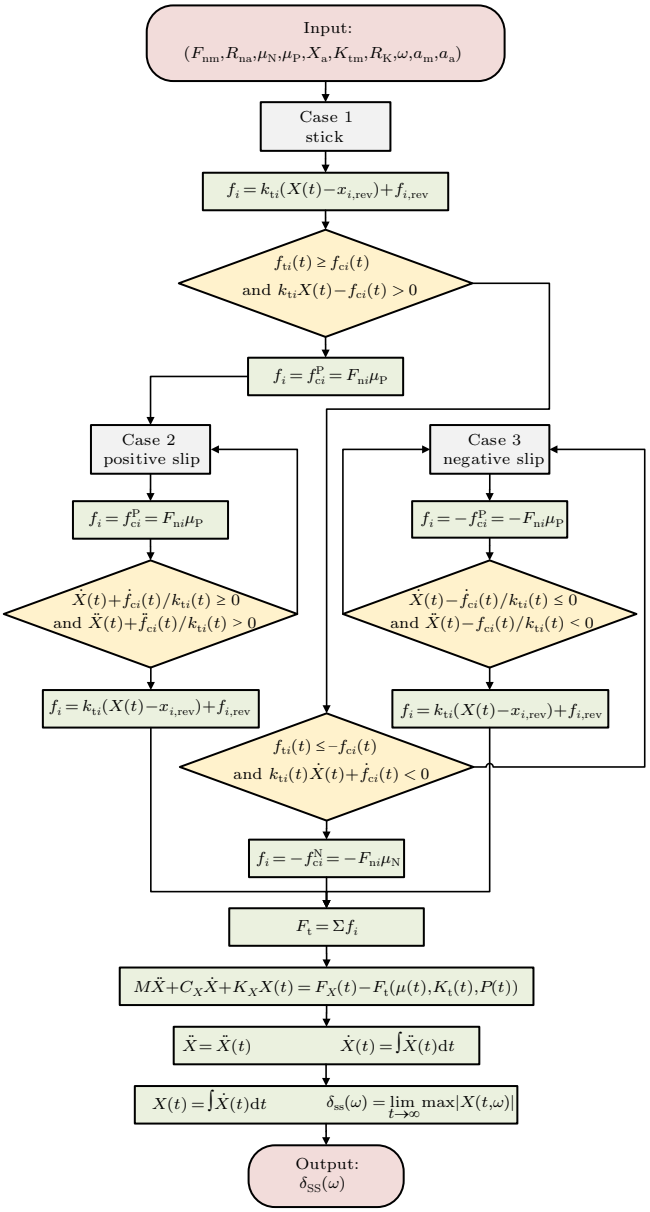


Fig. 6. Flowchart of the fretting friction model accounting for periodically varying stress distribution.

For frequencies below 120 Hz, the values of a_{m} and a_{a} exhibit minimal influence on the simulation outcomes. Through deliberate combinations of these parameters, optimal values for frequencies below 120 Hz were identified, as summarized

in Table 3. Conversely, at frequencies above 120 Hz, a_m and a_a exert a significantly greater influence on the simulation results — an effect that will be investigated in subsequent sections.

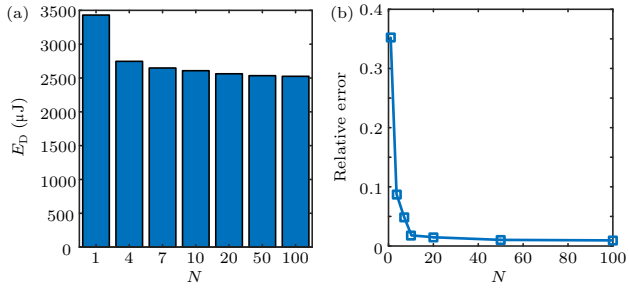


Fig. 7. Effect of the Jenkins element count on energy dissipation. (a) Dissipated energy for varying N. (b) Relative error for varying N.

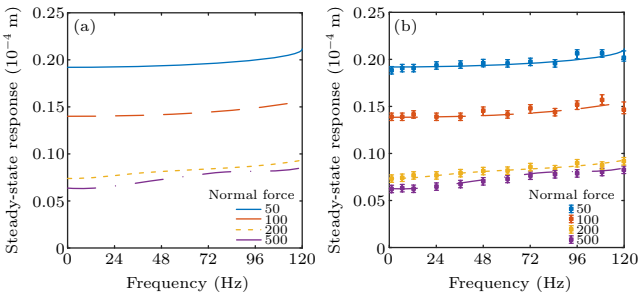


Fig. 8. Simulation and experimental results under varying normal forces at frequencies below 120 Hz. (a) Simulation results. (b) Comparison between experimental and simulated data.

Table 3. The R^2 for varying values of a_m and a_a.

a_m	a_a	R^2	a_m	a_a	R^2	a_m	a_a	R^2
0	0	0.947	0	0	0.947	0	0	0.947
0.5	0	0.957	0	0.5	0.958	0.5	0.5	0.961
1	0	0.955	0	1	0.954	1	1	0.956
2	0	0.952	0	2	0.948	2	2	0.944

Due to experimental constraints, fretting friction experiments with excitation frequencies exceeding 120 Hz could not be conducted. Therefore, for excitation frequencies above 120 Hz, the interfacial relative displacement influenced by non-uniform stress distribution was simulated using the fretting friction model.

4.2. Effect of stress distribution mean value coefficient on steady-state response

Set $N = 10$, $M = 9.988$ kg, $K_X = 1.013 \times 10^7$ N/m, $C_X = 202.236$ N·s/m, $K_{tm} = 3.006 \times 10^6$ N/m, $X_a = 2.842 \times 10^{-5}$ m, $\alpha = 45°$, $\mu_P = 0.36$, $\mu_N = 0.42$, $R_{F_Y} = 0.49$, $R_K = 0.13$, $\phi_{F_Y} = 0°$, $\phi_{F_X} = 0°$, $p_1 = 3.41 \times 10^4$, $p_2 = 3.88 \times 10^5$, $p_3 = 0.38$, $p_4 = 1.09$. The natural frequency of the system is $\omega_n = 159$ Hz. The upper limit of excitation frequency in simulation is 240 Hz.

The mean normal forces were set at 50 N, 100 N, 200 N, 500 N, 2000 N, and 10000 N. It should be noted that although the tangential stiffness increases with increasing normal force, the tangential stiffness of the interface cannot exceed that of the structure. When $K_t \geq K_X$, the interface displacement δ matches that of specimen 1, and relative motion ceases, i.e., $K_t = K_X$. At this stage, the interface transitions to a full-stick state accompanied by dominant plastic deformation. At normal forces of 2000 N and 10000 N, the interfacial pressure exceeds the yield strength of the experimental specimen. Consequently, structural strength becomes the primary factor governing vibrations. Simulations were performed to identify the system's second resonance frequency and to investigate amplitude variations near this frequency as functions of parameters a_m and a_a.

It should be noted that the nonlinearity of contact parameters mainly affects the viscous sliding section and the fully viscous section, and has a relatively small influence on the frequency response near the first resonance frequency. By varying the values of a_m, the following friction vibration simulation curves were obtained.

Under low normal force, specifically $F_{nm} = 50$ N, the interface exhibits full slip, with damping primarily arising from sliding friction energy dissipation, as shown in Fig. 9(a). The amplitude–frequency response features a high-amplitude peak near the first resonance frequency, while the frequency curve remains smooth due to negligible interface stiffness contribution and weak nonlinear effects.

Under medium normal forces, $F_{nm} = 100$ N and $F_{nm} = 200$ N, the interface enters mixed stick–slip states, where frictional hysteresis and stiffness fluctuations jointly govern the dynamics. The reduced proportion of sliding energy dissipation manifests as progressively diminishing amplitudes in the amplitude–frequency characteristics. When the mean normal force is $F_{nm} = 100$ N, the amplitude–frequency curve is shown in Fig. 9(b); the interface exhibits stick–slip behavior, though sliding remains dominant. Chaotic oscillations emerge at $F_{nm} = 200$ N, as shown in Fig. 9(c), where the interface approaches a critical stick–slip transition. Significant nonlinearities in contact parameters — specifically friction coefficient hysteresis and stiffness fluctuations — destabilize the amplitude–frequency response.

Under high normal forces, $F_{nm} = 500$ N, $F_{nm} = 2000$ N, and $F_{nm} = 10000$ N, the interface reaches a full-stick state dominated by interfacial stiffness, as shown in Figs. 9(d), 9(e), and 9(f). The amplitude–frequency characteristics exhibit a shift of the resonance frequency toward higher frequencies due to increased contact stiffness, which enhances the total system stiffness. Under heavy loading, the stronger coupling between interface stiffness and system modes causes the peak steady-state response to occur near the second resonance frequency.

As F_{nm} increases from 0 N to 200 N, the maximum response gradually decreases, with interfacial sliding behavior dominating this regime. Damping primarily arises from interfacial sliding. Under light loading conditions, the maximum

response diminishes with increasing normal force, mainly near the first resonance frequency. When F_{nm} increases from 200 N to 10000 N, the response gradually increases because stick contact becomes dominant, and the interface contributes additional stiffness to the system, raising the resonance frequency. Under heavy load conditions, the maximum response increases with increasing load, occurring near the second resonance frequency. The second resonance frequency rises with increasing normal force, primarily due to tangential stiffness changes induced by normal force variations. Notably, contact parameter nonlinearities predominantly affect the stick–slip and full-stick regimes, exerting minimal influence on the frequency response near the first resonance frequency.

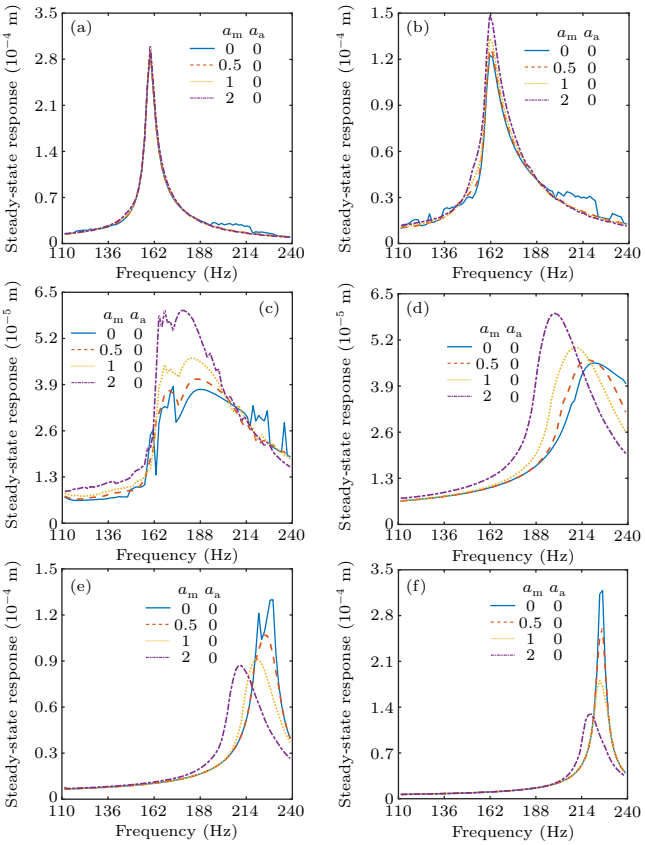


Fig. 9. Steady-state response for $a_a = 0$ with varying a_m: (a) $F_{nm} = 50$ N, (b) $F_{nm} = 100$ N, (c) $F_{nm} = 200$ N, (d) $F_{nm} = 500$ N, (e) $F_{nm} = 2000$ N, (f) $F_{nm} = 10000$ N.

4.3. Effect of stress distribution amplitude coefficient on steady-state response

When $a_m = 0$, the influence of a_a on the amplitude is shown in Fig. 10. When $F_{nm} = 50$ N, the effects of different a_a values on the amplitude (with $a_m = 0$) exhibit no significant difference compared with the effects of different a_m values on the amplitude when $a_a = 0$, as shown in Fig. 10(a).

When $F_{nm} = 100$ N and $a_m = 0$, the influence of varying a_a values on the amplitude is shown in Fig. 10(b). The peak interface response near the first resonance frequency is closer to that in Fig. 9(b). This behavior differs markedly from the influence of a_m on the interface response when $a_a = 0$. The difference arises because variations in a_a do not change the maximum value of the local contact stress at the interface.

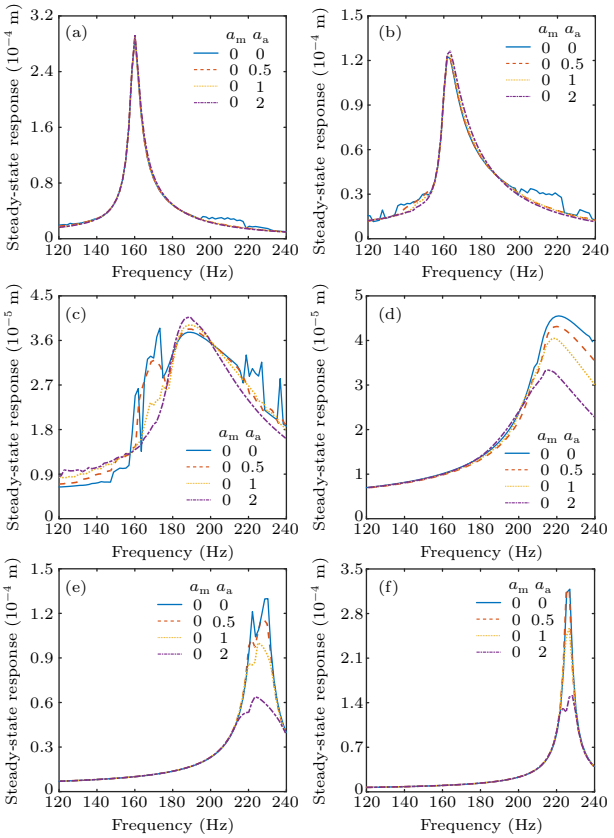


Fig. 10. Steady-state response for $a_m = 0$ with varying a_a: (a) $F_{nm} = 50$ N, (b) $F_{nm} = 100$ N, (c) $F_{nm} = 200$ N, (d) $F_{nm} = 500$ N, (e) $F_{nm} = 2000$ N, (f) $F_{nm} = 10000$ N.

When $F_{nm} = 200$ N, the influence of different a_a values on the amplitude (with $a_m = 0$) is shown in Fig. 10(c). Compared with Fig. 9(c), the peak values of the interface response near the first resonance frequency are closer, the maximum responses all decrease, and no nonlinear phenomenon occurs when $a_a = 2$.

When $F_{nm} = 500$ N, the influence of different a_a values on the amplitude (with $a_m = 0$) is shown in Fig. 10(d). In Fig. 11(d), the maximum responses, ranked from highest to lowest, correspond to $a_m = 2$ with $a_a = 0$, $a_m = 1$ with $a_a = 0$, $a_m = 0.5$ with $a_a = 0$, and $a_m = 0$ with $a_a = 0$. In Fig. 10(d), the maximum responses, ranked from highest to lowest, correspond to $a_m = 0$ with $a_a = 0$, $a_m = 0$ with $a_a = 0.5$, $a_m = 0$ with $a_a = 1$, and $a_m = 0$ with $a_a = 2$. Specifically, when $a_a = 0$, increasing a_m leads to an increase in the maximum response; conversely, when $a_m = 0$, increasing a_a results in a decrease in the maximum response. Compared with Fig. 9(d), the first resonance frequency where the maximum response occurs is closer. Larger normal forces lead to faster attainment of maximum response with increasing frequency; as the frequency increases further, the attenuation rate of the response also increases.

When F_{nm} is 2000 N and 10000 N, the influence of different a_a values on the amplitude (with $a_m = 0$) is shown in

Figs. 10(e) and 10(f), respectively. Compared with Figs. 9(e) and 9(f), the first resonance frequency where the maximum response occurs is closer for different a_a values. Moreover, larger normal forces cause the response to reach its maximum value more quickly as frequency increases, and further increases in frequency lead to faster attenuation of the response.

4.4. Effect of synchronous variation of stress distribution mean value coefficient and stress distribution amplitude coefficient on steady-state response

The interface response under synchronized variation of a_m and a_a is shown in Fig. 11. When $F_{nm} = 50$ N, the influence of synchronized variation of a_m and a_a on the amplitude-frequency curve is shown in Fig. 11(a), demonstrating no significant difference compared with Figs. 9(a) and 10(a).

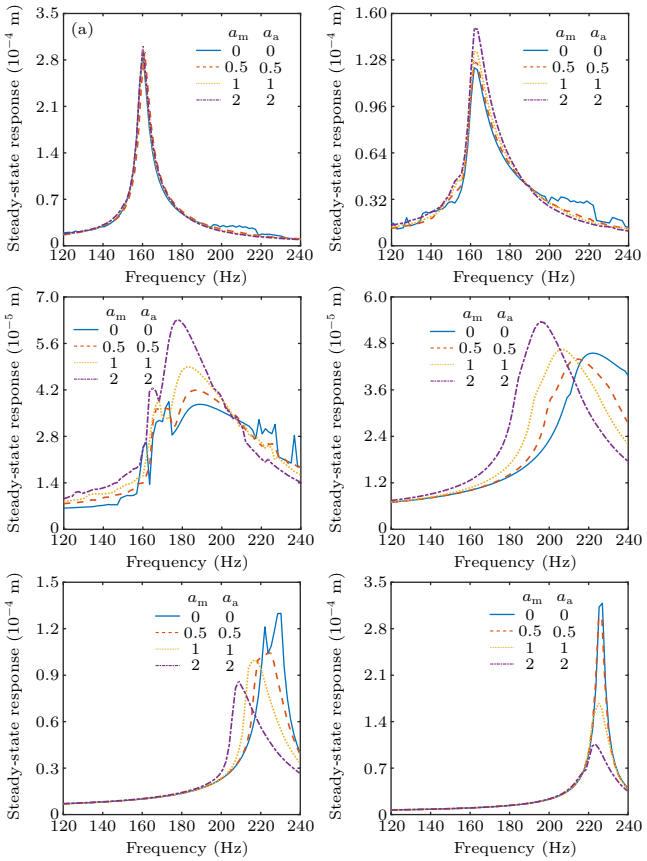


Fig. 11. Steady-state response for synchronized variation of a_m and a_a: (a) $F_{nm} = 50$ N, (b) $F_{nm} = 100$ N, (c) $F_{nm} = 200$ N, (d) $F_{nm} = 500$ N, (e) $F_{nm} = 2000$ N, (f) $F_{nm} = 10000$ N.

When $F_{nm} = 100$ N, the influence of synchronized variation of a_m and a_a on the amplitude-frequency curve is shown in Fig. 11(b). Stronger nonlinear characteristics in the interface stress distribution lead to more pronounced nonlinear behavior in the interface response compared with Figs. 9(b) and 10(b).

When $F_{nm} = 200$ N, the influence of synchronized variation of a_m and a_a on the amplitude-frequency curve is shown in Fig. 11(c). Figures 9(c), 10(c), and 11(c) all exhibit highly nonlinear behavior.

When $F_{nm} = 500$ N, the influence of synchronized variation of a_m and a_a on the amplitude-frequency curve is shown in Fig. 11(d). In Fig. 11(d), the maximum responses, ranked from highest to lowest, correspond to $a_m = 2$ with $a_a = 2$, $a_m = 1$ with $a_a = 1$, $a_m = 0$ with $a_a = 0$, and $a_m = 0.5$ with $a_a = 0.5$. When a_m and a_a increase synchronously, the maximum response first decreases and then increases. Compared with Figs. 9(d) and 10(d), the first resonance frequencies where the maximum responses occur are most dispersed, and the separation between curves increases most rapidly with increasing normal force.

When F_{nm} is 2000 N and 10000 N, the influence of synchronized variation of a_m and a_a on the amplitude is shown in Figs. 11(e) and 11(f), respectively. Compared with Figs. 9(e), 9(f), 10(e), 10(f), 11(e), and 11(f) exhibit the weakest nonlinear characteristics. In Fig. 11(e), the frequencies corresponding to different maximum responses are most dispersed, while in Fig. 11(f), they are most concentrated.

4.5. Fretting friction simulation of slip-stick state transition

According to the results calculated by the vibration response analysis program, when the average normal excitation force is 200 N, the amplitude-frequency curve exhibits strong nonlinearity. Therefore, we analyzed the amplitude-frequency curves near a normal excitation of 200 N and designed three groups of controlled experiments.

Under the condition $a_m = 0$ and $a_a = 0$, the first group calculates the response for normal excitations of 185 N, 190 N, 195 N, 200 N, 205 N, 210 N, and 215 N, with a frequency sweep from 120 Hz to 240 Hz, as shown in Fig. 12.

As the frequency increases, the steady-state response rises gradually, undergoes nonlinear fluctuations, reaches a peak, and then declines slowly while exhibiting further nonlinear oscillations.

Based on the findings in Subsection 4.1, the coefficient of determination R^2 reaches its maximum when $a_m = 0.5$ and $a_a = 0.5$. Consequently, the second and third group simulations were conducted under the condition $a_m = 0.5$ and $a_a = 0.5$, focusing on the parameter range near $F_{nm} = 200$ N.

The second group calculates the response for normal excitations of 185 N, 190 N, 195 N, 200 N, 205 N, 210 N, and 215 N, with a frequency range from 120 Hz to 240 Hz, as shown in Fig. 13. The steady-state response-frequency curve for the second group ($a_m = 0.5$ and $a_a = 0.5$) exhibits greater stability than that for the first group ($a_m = 0$ and $a_a = 0$). Interestingly, more uniform stress distribution results in more pronounced amplitude fluctuations of the relative displacement (in the frequency domain), challenging the conventional understanding that uniform stress promotes stability. The curves exhibit distinct stage differentiation.

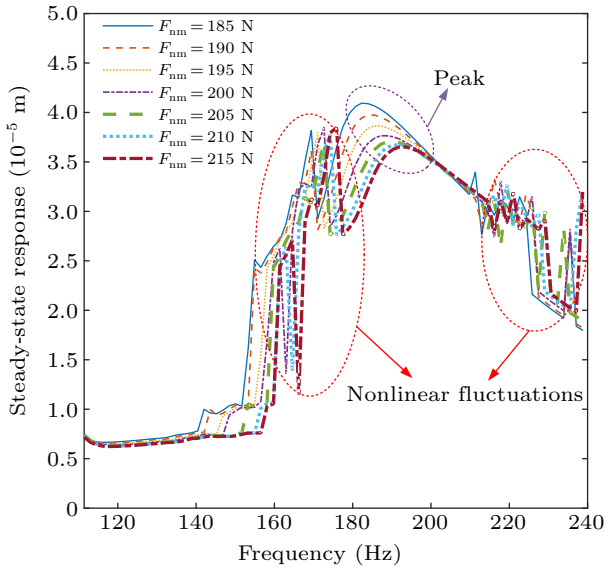


Fig. 12. Steady-state response for $a_m = 0$ and $a_a = 0$, with mean normal force varying from 185 N to 215 N.

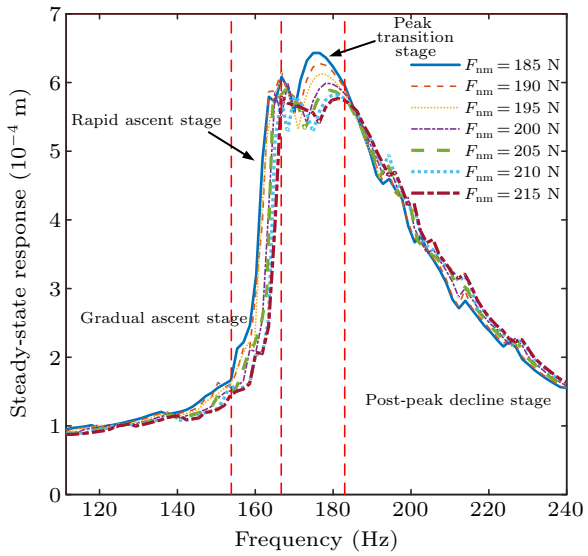


Fig. 13. Steady-state response for $a_m = 0.5$ and $a_a = 0.5$, with mean normal force varying from 185 N to 215 N.

(i) Gradual ascent stage (120–150 Hz): At low frequencies, the excitation energy is insufficient to trigger stick-slip state transitions. The interface remains predominantly in the slip state, with limited influence from uneven stress distribution. Curves for different mean normal forces exhibit strong coincidence. The steady-state response increases gradually with frequency, showing no significant nonlinearity.

(ii) Rapid ascent stage (150–170 Hz): As frequency approaches the first resonance frequency, the response arises from the superposition of the stick state in high-pressure contact zones and the slip state in low-pressure zones. Higher tangential stiffness in high-pressure zones results in elevated local natural frequencies, driving these regions into a pre-critical stick-resonance state. Lower tangential stiffness in low-pressure zones maintains slip-dominated friction. The global response features coupled multi-frequency ascent, characterized by the coexistence of incipient stick resonance and prevailing slip states, with displacement rising rapidly with frequency.

(iii) Peak transition stage (170–190 Hz): Stick dominates high-pressure zones, while discrete dissipation from sliding friction persists in low-pressure zones. Their coupling causes the steady-state response to first rise, then decline, and subsequently rise to its peak. In high-pressure zones, viscoelastic contact leads to energy dissipation efficiency initially increasing and then decreasing with rising frequency, producing the initial ascent-descent trend. In low-pressure zones, continuous sliding friction dissipates energy, preventing unlimited displacement growth. Peak amplitude occurs when energy input and dissipation reach equilibrium.

(iv) Post-peak decline stage (190–240 Hz): At higher frequencies, the energy dissipation efficiency decreases with increasing frequency. Stick dissipation efficiency declines in high-pressure zones, while the contribution of sliding friction recovers in low-pressure zones. Sliding friction (frequency-independent) causes displacement to decrease smoothly with frequency. Discrete slip effects are averaged at high frequencies, eliminating significant fluctuations in the amplitude-frequency curve.

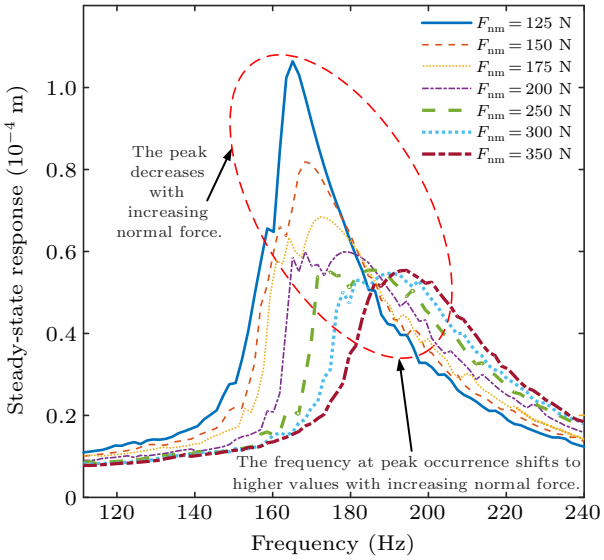


Fig. 14. Steady-state response for $a_m = 0.5$ and $a_a = 0.5$, with mean normal force varying from 125 N to 350 N.

The third group calculated the response of normal excitation from 125 N, 150 N, 175 N, 200 N, 250 N, 300 N, 350 N, and the frequency from 120 Hz to 240 Hz, as shown in Fig. 14. It was observed that the amplitude curves of normal excitation between 185 N and 215 N exhibit similar spurious fluctuations, while the amplitude curves gradually smooth out as the normal excitation decreases from 200 N to 125 N and increases from 200 N to 350 N. This clearly suggests that the interface is particularly prone to the stick-slip phenomenon when the normal excitation is around 200 N, indicating a criti-

cal and highly sensitive state of dynamic frictional behavior at the contact interface.

When the amplitude of normal force fluctuation is large, the frequency at which the peak occurs increases with increasing normal force (stiffness-dominated behavior), and the steady-state response displacement at the peak decreases with increasing normal force (dissipation-dominated behavior). Stick-slip state transitions at the contact interface simultaneously exhibit both spatial asynchronicity (different contact areas display different stick-slip states at the same time due to pressure gradients) and temporal asynchronicity (phase fluctuations in the timing of periodic stick-slip state switching within the same area under dynamic stress cycles), forming a complex and intricate spatiotemporal dual-dimensional stick-slip coupling. The frequency difference between stick-slip transitions in high-pressure regions (high stiffness) and low-pressure regions (low stiffness) is denoted as Δf_{space}, and the frequency difference between the excitation-induced dynamic stress frequency and the dynamic restructuring frequency of contact spots is denoted as Δf_{time}. When Δf_{space} closely matches Δf_{time}, the energy dissipation efficiency during stick-slip transitions is significantly enhanced, nonlinear fluctuations in the amplitude-frequency curve increase, and the frequency components become more complex, richer, and widely distributed in detail.

The amplitude-frequency curves exhibit strong nonlinear fluctuations under normal excitation around 200 N. The reasons for this can be attributed to the following:

(i) Critical state of the stick-slip phenomenon.

When the normal excitation is close to 200 N, the interface is in a critical state, transitioning from slip-dominance (low normal force) to stick-dominance (high normal force). The interface frequently switches between stick (static friction) and slip (dynamic friction), resulting in discontinuous friction jumps. This dynamic instability directly triggers pronounced and unpredictable random fluctuations in amplitude.

(ii) Non-uniformity of stress distribution.

Simulation of the equivalent stress distribution function (power function) reveals that the stress distribution exhibits significant non-uniformity around 200 N. Local stress concentration regions reach the slip condition first, while adjacent areas remain in stick state, forming partial slip. This spatial heterogeneity exacerbates the nonlinearity of energy dissipation, resulting in more irregular, complex, and highly sensitive fluctuations in the response curve.

(iii) Coupling effect of nonlinear contact parameters.

The improved IwanN model integrates tangential stiffness fluctuations, frictional hysteresis, and stress distribution variations. Near 200 N, these nonlinear parameters may reach the peak of their synergistic effect. Changes in normal force cause dynamic adjustment of the interface contact stiffness, resulting in a resonant frequency shift. The directional dependence of the friction force during stick-slip further exacerbates the asymmetry of energy dissipation. These combined effects amplify the overall complexity and richness of the system response.

(iv) Limitations of the dynamic properties of the experimental setup.

Fluctuations around 200 N occur mainly in the low- and mid-frequency bands. In this range, the system is more sensitive to nonlinear variations in contact parameters, and experimentally observed fluctuations may result from the coupling of the device's dynamic characteristics with the nonlinear behavior of the interface. Control experiments show that fluctuations are significant when the normal excitation is in the range of 185–215 N, while the curve tends to be smooth when the normal excitation is far from 200 N, directly verifying the existence of the critical state and confirming the highly sensitive nature of the interface dynamics.

IwanN[17] model simulations show that stress distribution inhomogeneity significantly affects the flatness of the amplitude curve, supporting the role of non-uniform stresses. The theory of Menq[5] states that energy dissipation in the stick-slip state is dynamically related to the normal force, and the vicinity of 200 N lies in the transition interval dominated by stick-slip, consistent with the interpretation of the critical state.

Taken together, the spurious fluctuation near 200 N is a combined result of the dynamic properties of the interface (stick-slip transition), the non-uniformity of the stress distribution, and the coupling effect of nonlinear contact parameters. This phenomenon reveals the complex and highly sensitive dynamic behavior of the mechanical contact interface under critical load, providing an important reference for high-precision vibration control, damping design, and mechanical reliability studies.

The rule that the normal contact force governs interfacial contact states (full slip — partial slip — full stick), as established in this study, is applicable under the specific experimental conditions and material combinations employed. The detailed scope of applicability is defined as follows:

Material combination: The conclusion has been validated for contact pairs consisting of PMMA and SUS304, which are widely used in mechanical interface research. For material pairs with substantially different mechanical properties, the critical normal force for contact state transition may vary. Differences in elastic modulus, yield strength, and intrinsic friction coefficient influence the actual contact area and interfacial friction resistance, necessitating further experimental verification.

Surface roughness: The surface roughness of the specimens in this study was controlled within the range of *Ra* 0.01–1.6 μm, consistent with typical machining standards for me-

chanical structural components. For surfaces with extremely low roughness ($Ra < 0.01$ μm, e.g., polished surfaces), the interlocking effect between asperities is weakened, which may enhance the tendency for slip and increase the critical normal force required for the transition to the stick state. Conversely, for surfaces with high roughness ($Ra > 1.6$ μm, e.g., rough cast surfaces), local stress concentrations become more pronounced, potentially promoting early stick behavior and reducing the critical normal force for state transition.

Excitation frequency range: Experimental validation and simulation analyses were conducted within an excitation frequency range of 2–240 Hz, covering typical vibration frequencies encountered in critical mechanical interfaces such as aero-engine blade roots and automotive transmission joints. At frequencies exceeding 240 Hz, inertial effects at the contact interface and bandwidth limitations of the piezoelectric actuator (a core component of the test system) may introduce deviations in the measurement of contact forces and relative displacements, affecting the determination of contact states. At frequencies below 2 Hz, creep deformation of PMMA becomes increasingly significant, altering the normal force distribution across the interface and modifying the transition behavior among contact states.

Beyond the above ranges, additional experiments and adjustments to model parameters are required to ensure the reliability of the conclusions.

5. Conclusion

Based on the above analysis, the following conclusions can be drawn.

First, interfacial stress nonuniformity directly governs vibration response irregularity. Compared to non-uniform stress distribution, uniform stress distribution leads to less stable stick-slip transitions and amplifies the steady-state relative displacement response at the contact interface observed in frequency-domain characteristics.

Second, distinct vibration anomalies emerge near the stick-slip transition threshold, attributed to the coupled effects of stress heterogeneity, friction hysteresis, and tangential stiffness variations during state transitions.

Third, the magnitude of the normal contact force systematically shifts vibration dominance regimes: Under lower normal force, the interface contact state is full slip; under higher normal force, the interface contact state becomes partial slip; and with further increases in normal force, the interface contact state transitions to full stick. Lower normal forces lead to slip-dominated energy dissipation, characterized by peak response at the first resonance frequency, whereas higher normal forces induce stick-dominated energy dissipation, characterized by peak response at the second resonance frequency.

Based on the established fretting friction model, this study quantitatively analyzes the influence of dynamic contact interface stress distribution on the steady-state response of the contact interface as the frequency increases from low to high, and explains the underlying mechanisms. The stress distribution at the contact interface affects not only the magnitude of the peak steady-state response but also the frequency at which the steady-state response occurs. This work provides a foundational framework for predicting and controlling vibration in jointed structures subjected to dynamic interfacial loading.

Acknowledgments

Project supported by the National Natural Science Foundation of China (Grant No. 11872033) and the Beijing Natural Science Foundation, China (Grant No. 3172017).

References

[1] Briscoe B J 1985 *Tribol. Int.* **18** 198
[2] Asai K and Gola M M 2015 *ASME Turbo Expo.*, June 15–19, 2015, Montréal, Canada, V07BT33A002
[3] Pesaresi L, Salles L, Jones A, Green J S and Schwingshackl C W 2017 *Mech. Syst. Signal Process.* **85** 662
[4] Pesaresi L, Salles L, Elliott R, Jones A, Green J S and Schwingshackl C W 2016 *AMM* **849** 1
[5] Menq C H and Yang B D 1998 *J. Sound Vib.* **217** 127
[6] Joannin C, Chouvion B, Thouverez F, Mbaye M and Ousty J P 2016 *J. Eng. Gas Turbines Power* **138** 072504
[7] She H, Li C, Tang Q and Wen B 2020 *Shock Vib.* **2020** 7604174
[8] Zhao W, Zhang D and Xie Y 2019 *J. Low Freq. Noise Vib. Act. Control* **38** 1505
[9] Asai K, Kudo T and Yoda H 2014 *J. Eng. Gas Turbines Power* **136** 042101
[10] Segalman J D 2006 *Struct. Control Health Monit.* **13** 430
[11] Vingsbo O and Soderberg B 1988 *Wear* **126** 131
[12] Goodman L E 1980 *ASME Appl. Mech. Div. AMD* **39** 1
[13] Usta A D, Shinde S and Eriten M 2017 *J. Tribol.* **139** 061402
[14] Xiao H, Shao Y and Xu J 2014 *Eur. J. Mech. A Solids* **43** 1
[15] Valanis K C 1980 *Arch. Mech.* **32** 68
[16] Wen Y K 1976 *J. Eng. Mech., ASCE* **12** 249
[17] Iwan W D 1964 *J. Appl. Mech.* **34** 612
[18] Song Y, Hartwigsen C J, McFarland D M, Vakakis A F and Bergman L A 2004 *J. Sound Vib.* **273** 249
[19] Argatov I I and Butcher E A 2011 *J. Non-Linear Mech.* **46** 347
[20] Parker R C and Hatch D 2002 *Proc. Phys. Soc.* **63** 185
[21] Bhushan B 1985 *ASME/ASLE Trans.* **28** 181
[22] Maegawa S, Itoigawa F and Nakamura T 2016 *Tribol. Lett.* **62** 15
[23] Maegawa S, Itoigawa F and Nakamura T 2016 *Tribol. Int.* **93** 182
[24] Maegawa S, Itoigawa F and Nakamura T 2016 *Tribol. Int.* **102** 532
[25] Maegawa S, Itoigawa F and Nakamura T 2015 *J. Adv. Mech. Des. Syst.* **9** JAMDSM0069
[26] Song B, Yan S and Xiang W 2015 *Chin. Phys. B* **24** 014601
[27] Song B and Yan S 2017 *Chin. Phys. B* **26** 074601
[28] Luo Z, Song B, Han J and Yan S 2019 *Chin. Phys. B* **28** 054601
[29] Luo Z, Song B, Han J and Yan S 2019 *Chin. Phys. B* **28** 104601
[30] Han J, Luo Z, Zhang Y and Yan S 2021 *Chin. Phys. B* **30** 054601
[31] Han J, Ding J, Wu H and Yan S 2022 *Chin. Phys. B* **31** 034601
[32] Lu S, Han J and Yan S 2023 *Chin. Phys. B* **32** 044602
[33] Feng Y, Wu S, Nie H, Peng C and Wang W 2024 *Ind. Lubr. Tribol.* **76** 1108
[34] Rubinstein S M, Cohen G and Fineberg J 2004 *Nature* **430** 1005
[35] Sanliturk K Y and Ewins D J 1996 *J. Sound Vib.* **193** 511